the HHG spectrum (*14*, *21*–*23*). This is the primary reason for the relative enhancement of the HOMO-1 component of the HHG signal in our experiment. The model in (*21*) applied to the antisymmetric HOMO-1 predicts an HHG enhancement for the condition $\Delta = \lambda_{dB}/2$, where Δ is the separation between the two antinodes in the wave function along the direction of the returning electron **k**-vector. For a prolate molecular distribution, the prominent direction is $\alpha = 90°$, which results in $\Delta = 1.74$ bohr. The electron recombines, releasing a photon whose energy is equal to the sum of the electron kinetic energy and the ionization potential, and so this λ_{dB} of 3.48 bohr leads to a maximum at 60 eV in the emitted spectrum. For molecules with smaller α, which are also present in the prolate distribution, Δ becomes larger. This results in a shift of the constructive interference to larger λ_{dB} and smaller photon energies. Therefore, we expect a strong contribution from the HOMO-1 in the energy range around and below 60 eV, as seen in Fig. 3B. The cutoff for our intensities lies in this energy range, and we observe an agreement between the calculation and the data in Fig. 3. The full width at half maximum of the HOMO-1 spectrum in the constructive interference region is 20 eV for the highest I_G and about 10 eV for the lowest I_G. This trend agrees with the experiment: The HOMO-1 feature is prominent from harmonic 25 to harmonic 39, corresponding to a width of 22 eV for the highest I_G; for the lowest I_G, the peak appears from harmonic 25 to harmonic 31, corresponding to a width of 9 eV.

Note added in proof: We expect that the multiorbital contributions in HHG are general, which is supported by recent conference reports on HHG in CO_2 (*24*, *25*).

References and Notes

1. J. Itatani *et al.*, *Nature* **432**, 867 (2004).
2. P. B. Corkum, *Phys. Rev. Lett.* **71**, 1994 (1993).
3. K. C. Kulander, K. J. Schafer, J. L. Krause, *Laser Phys.* **3**, 359 (1993).
4. H. Stapelfeldt, T. Seideman, *Rev. Mod. Phys.* **75**, 543 (2003).
5. Th. F. Gallagher, *Rydberg Atoms* (Cambridge Univ. Press, Cambridge, 1994).
6. X. M. Tong, Z. X. Zhao, C. D. Lin, *Phys. Rev. A* **66**, 033402 (2002).
7. M. J. Frisch *et al.*, Gaussian 03, Revision C.02 (Gaussian Inc., Wallingford, CT, 2004).
8. V. I. Usachenko, S. I. Chu, *Phys. Rev. A* **71**, 063410 (2005).
9. M. Spanner, O. Smirnova, P. B. Corkum, M. Y. Ivanov, *J. Phys. B* **37**, L243 (2004).
10. J. Levesque *et al.*, *Phys. Rev. Lett.* **99**, 243001 (2007).
11. P. Balcou, P. Salières, A. L'Huillier, M. Lewenstein, *Phys. Rev. A* **55**, 3204 (1997).
12. S. Ramakrishna, T. Seideman, *Phys. Rev. Lett.* **99**, 113901 (2007).
13. P. Salières, A. L'Huillier, M. Lewenstein, *Phys. Rev. Lett.* **74**, 3776 (1995).
14. X. Zhou *et al.*, *Phys. Rev. Lett.* **100**, 073902 (2008).
15. A. T. Le, X.-M. Tong, C. D. Lin, *Phys. Rev. A* **73**, 041402 (2006).
16. P. Liu *et al.*, *Phys. Rev. A* **78**, 015802 (2008).
17. M. Gühr, B. K. McFarland, J. P. Farrell, P. H. Bucksbaum, *J. Phys. B* **40**, 3745 (2007).
18. J. Ortigoso, M. Rodriguez, M. Gupta, B. Friedrich, *J. Chem. Phys.* **110**, 3870 (1999).
19. J. Levesque, D. Zeidler, J. P. Marangos, P. B. Corkum, D. M. Villeneuve, *Phys. Rev. Lett.* **98**, 183903 (2007).
20. D. Pavičić, K. F. Lee, D. M. Rayner, P. B. Corkum, D. M. Villeneuve, *Phys. Rev. Lett.* **98**, 243001 (2007).
21. M. Lein, N. Hay, R. Velotta, J. P. Marangos, P. L. Knight, *Phys. Rev. A* **66**, 023805 (2002).
22. T. Kanai, S. Minemoto, H. Sakai, *Nature* **435**, 470 (2005).
23. C. Vozzi *et al.*, *Phys. Rev. Lett.* **95**, 153902 (2005).
24. O. Smirnova *et al.*, in *11th International Conference on Multiphoton Processes*, J. Anton *et al.*, Eds. (MPI für Kernphysik, Heidelberg, 2008), p. 7.
25. Y. Mairesse *et al.*, in *11th International Conference on Multiphoton Processes*, J. Anton *et al.*, Eds. (MPI für Kernphysik, Heidelberg, 2008), p. Fr62.

26. We thank H. Merdji and O. Smirnova for insightful discussions. Supported by the U.S. Department of Energy Division of Basic Energy Sciences through the Stanford Linear Accelerator Center, and by a Humboldt Foundation fellowship (M.G.).

7 July 2008; accepted 16 September 2008
Published online 30 October 2008;
10.1126/science.1162780
Include this information when citing this paper.

Radar Sounding Evidence for Buried Glaciers in the Southern Mid-Latitudes of Mars

John W. Holt,[1]* Ali Safaeinili,[2] Jeffrey J. Plaut,[2] James W. Head,[3] Roger J. Phillips,[4] Roberto Seu,[5] Scott D. Kempf,[1] Prateek Choudhary,[1] Duncan A. Young,[1] Nathaniel E. Putzig,[4] Daniela Biccari,[5] Yonggyu Gim[2]

Lobate features abutting massifs and escarpments in the middle latitudes of Mars have been recognized in images for decades, but their true nature has been controversial, with hypotheses of origin such as ice-lubricated debris flows or glaciers covered by a layer of surface debris. These models imply an ice content ranging from minor and interstitial to massive and relatively pure. Soundings of these deposits in the eastern Hellas region by the Shallow Radar on the Mars Reconnaissance Orbiter reveal radar properties entirely consistent with massive water ice, supporting the debris-covered glacier hypothesis. The results imply that these glaciers formed in a previous climate conducive to glaciation at middle latitudes. Such features may collectively represent the most extensive nonpolar ice yet recognized on Mars.

In equatorial regions of Mars, steep slopes (e.g., massifs and channel walls) typically exhibit talus fans and cones at their bases. In the martian mid-latitudes, however, many massifs are instead accompanied by broad, lobate aprons extending up to ~20 km away from their bases (*1*). They are characterized by gently sloping surfaces with convex-upward margins, relatively steep outer edges, and both radial and concentric ridge-and-furrow lineations (*2*); these features all indicate flow of a viscous material. Such "lobate debris aprons" (LDAs) occur in the 30° to 60° latitude belts in both hemispheres (Fig. 1A), concentrated in the north along the topographic dichotomy and in the south around massifs on the rims of the Hellas and Argyre basins (*2*). These latitudinal bands correlate with the shallow-subsurface stability field for water ice (i.e., ice could exist just below the surface but would sublimate at the surface) (*3*, *4*). Additionally, the flow-like morphology of the lobes suggests the presence of a viscosity-lowering agent such as ice (*2*, *4*).

Opinions differ, however, on the origin and amount of such ice and its mode of emplacement. Some propose that ancient ground ice was mobilized during LDA formation (*5*); others suggest that frost deposited from the atmosphere diffused into pore spaces (*2*), lubricating the debris deposits derived from nearby steep slopes and forming something akin to terrestrial rock glaciers (*6*). Different approaches have been used to estimate the amount of ice within LDAs. At a minimum, ice volumes on the order of ~10 to 15% are required to mobilize talus (*2*). However, surface pitting and structures suggest that the ice content is more than 50% for some LDAs (*7*). This estimate is also consistent with those based on detailed topographic profiles (*8*, *9*) and rheological arguments (*10*). Some terrestrial analogs (*11*–*13*) suggest that LDAs might be debris-covered glaciers, essentially pure glacial ice below a protective layer of debris. Superposed rimless craters with broad central peaks and moat-shaped borders indicate formation on an ice-rich substrate (*14*). However, the presence of massive ice (or very ice-rich mixtures) is impossible to confirm or reject on the basis of optical imagery or surface morphology alone.

We used the Shallow Radar (SHARAD) (*15*) on the Mars Reconnaissance Orbiter (MRO) to probe the internal structure of several LDAs sur-

[1]Institute for Geophysics, Jackson School of Geosciences, University of Texas, Austin, TX 78758, USA. [2]Jet Propulsion Laboratory, California Institute of Technology, Pasadena, CA 91109, USA. [3]Department of Geological Sciences, Brown University, Box 1846, Providence, RI 02912, USA. [4]Southwest Research Institute, Boulder, CO 80302, USA. [5]INFOCOM Department, University of Rome "La Sapienza," 00184 Rome, Italy.

*To whom correspondence should be addressed. E-mail: jack@ig.utexas.edu

rounding massifs on the eastern rim of the Hellas impact basin (Fig. 1) where more than 90 LDA complexes flank steep topography (*2*, *6*, *16*). The southernmost LDA we studied (LDA-2, Fig. 1B) has multiple lobes that coalesce to form a continuous deposit extending more than 20 km outward from a massif along ~170 km of its margins. Surface features indicating viscous flow are numerous, including both longitudinal and transverse lineations (*16*) (Fig. 2).

Radar waves penetrate the surface and pass through materials that do not severely attenuate or scatter them. Reflections arise from interfaces with dielectric contrasts. SHARAD has penetrated the ~2-km-thick polar layered deposits in both the north and south, detecting many internal reflectors (*17*, *18*). Smaller targets can be more challenging because SHARAD's antenna pattern is broad, resulting in surface reflections up to a few tens of kilometers away from the suborbital point in rugged areas, versus only a few kilometers in smooth, flat areas. These off-nadir echoes can appear at time delays similar to those arising from subsurface interfaces, so steps are required to avoid misinterpreting this surface clutter as subsurface echoes. Synthetic-aperture data processing is used to improve along-track resolution to ~300 m, greatly reducing along-track clutter and focusing the surface and subsurface features. We used the known topography of the surface and the radar geometry to model cross-track clutter together with nadir surface echoes (see supporting online text). Comparisons of radar sounding data with these synthetic surface echoes and the examination of possible surface echo sources in imagery (*19*) were undertaken for all cases shown here; such a procedure is a necessary part of radar sounding data interpretation in high-relief environments.

Examination of radar data from SHARAD orbit 6830 where it crosses multiple LDAs in the eastern Hellas region (a-a′, Fig. 1B) shows that the only radar reflections not matching simulated surface echoes occur where the spacecraft passes over each LDA (Fig. 3, A and B); therefore, these echoes are interpreted as arising from within or beneath the LDAs. In one case (LDA-2A), surface clutter is predicted near the terminus of the LDA, where it may obscure portions of a subsurface reflector that clearly extends farther inward below the LDA. LDA-2A and LDA-2B show evidence for multiple, closely spaced subsurface reflectors indicating the presence of at least one thin (~70 m assuming a water-ice composition), distinct deposit below thicker deposits (up to 800 m).

Another criterion for the interpretation of subsurface echoes is consistency between multiple tracks. Orbit 7219 (Fig. 1B, b-b′) crosses LDA-2A and LDA-2B near orbit 6830 (Fig. 1B, a-a′) but at a different angle. The secondary echoes in orbit 7219 (Fig. 4, A to C) are nearly identical to those observed for orbit 6830 (Fig. 3, right side). The nearby crossing of LDA-2C by orbit 3672 (Fig. 1B, c-c′) shows overall consistency across different lobes of this LDA complex while exhibiting slightly varying details of the subsurface. LDA-2C is characterized by what appears to be a more extensive basal deposit relative to LDA-2B. This was observed in additional nearby crossings.

SHARAD is capable of resolving reflections separated by ~0.1 μs in time (i.e., ~10 m in ice or ~5 m in rock), yet there are no indications of structure within the LDAs apart from thin deposits near the base. Hints of potential internal reflectors within the LDAs can all be correlated with surface clutter in the simulated data (e.g., LDA-1 and LDA-2B; Fig. 3). There is also an apparent lack of volume scattering (i.e., radar reflectors dispersed throughout the material) at SHARAD frequencies. Although some dispersed energy follows LDA surface echoes, we attribute this to small-scale surface roughness such as that visible in imagery (Fig. 2), as it is not noticeably different in the radar data from nearby LDA-free

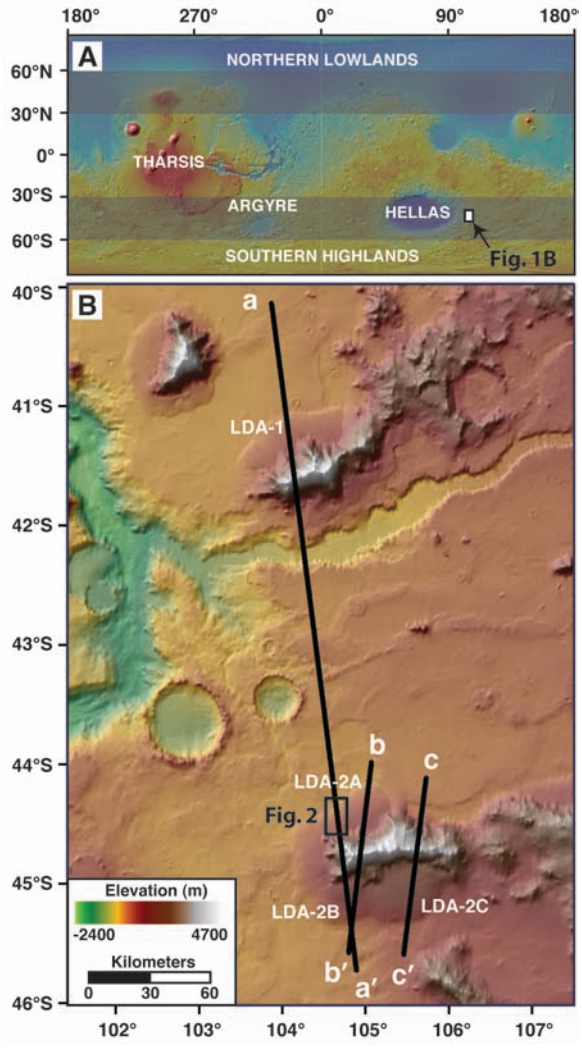

Fig. 1. (**A**) Topography of Mars (*24*). Major features are identified, and latitude bands exhibiting lobate debris aprons (LDAs) and lineated valley fill are highlighted (*1*, *2*). The location of our study area along the eastern rim of the Hellas impact basin is also denoted. (**B**) Topography of study area, with MRO/SHARAD ground tracks shown for orbits 6830 (a-a′), 7219 (b-b′), and 3672 (c-c′). LDAs crossed by these tracks are labeled.

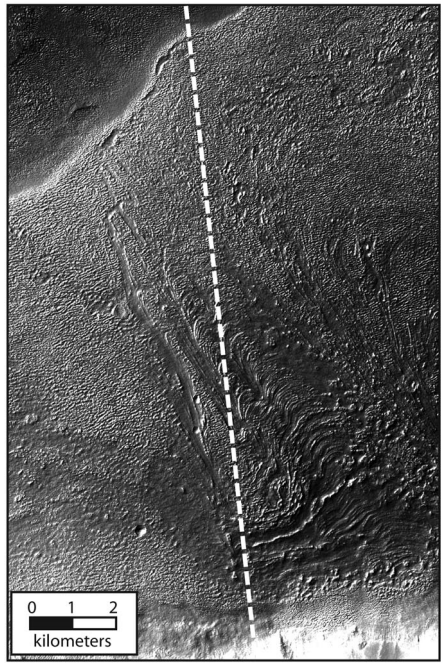

Fig. 2. Image showing surface of LDA-2A where it is crossed by orbit 6830 (see Fig. 1B for location). Textures visible include transverse and longitudinal ridge-and-furrow lineations indicative of viscous flow. [From MRO Context Camera image P01_002294_1349]

areas (Fig. 1 and Fig. 3B) and is supported by simulations (Fig. 3A and Fig. 4, A and D). These properties of the radar data indicate that (i) the material is largely homogeneous, and (ii) it lacks a significant fraction of large (i.e., several meters across or larger) rock fragments. Both characteristics support the debris-covered glacier hypothesis.

A further constraint on composition comes from the measured loss of radar energy through the material. We measured the correlation between the strength of the subsurface echo and the delay between the upper and lower echo (or, equivalently, the thickness of the medium). It is expected that there will be a proportional drop in the subsurface echo strength as the depth to the bed increases. The radar attenuation had an upper bound of ~10 dB/km (fig. S1). This is consistent with radar attenuation by relatively pure water ice, rather than by a rock-dominated composition (*20*), and is supported by Mars-analog laboratory studies of water-ice mixtures with basaltic dust indicating that a dust fraction higher than 10% is unlikely for losses of this magnitude (*21*).

As a check on this interpretation, we used the velocity of electromagnetic waves in water ice (real dielectric constant of 3.2) to convert the time-delay data into depth. The resulting basal geometries (Fig. 3C and Fig. 4, C and F) show a lower interface that smoothly continues the general trend of the nearby surface, with a slight slope in some cases (up to 1.5°) toward the adjacent massif. Some increased slope relative to the surroundings is consistent with the proximal buildup of colluvium from high topography before the deposition of the ice-rich material, or a sublimation lag from an older ice-rich deposit. The combination of a low radar attenuation and an implied water-ice radar velocity is similar to the findings for the polar layered deposits by the Mars Advanced Radar for Subsurface and Ionospheric Sounding (MARSIS) radar sounder on the Mars Express orbiter (*22*, *23*). As in those cases, our results point to a composition dominated by ice with perhaps a small fraction of dust or rock, rather than typical rock-dominated deposits or rock-ice mixtures with a roughly equal distribution.

All of these radar-based observations indicate that LDAs consist of massive ice covered by a relatively thin debris layer. The thickness of the surface debris layer cannot be observed because the vertical resolution of the radar is too limited

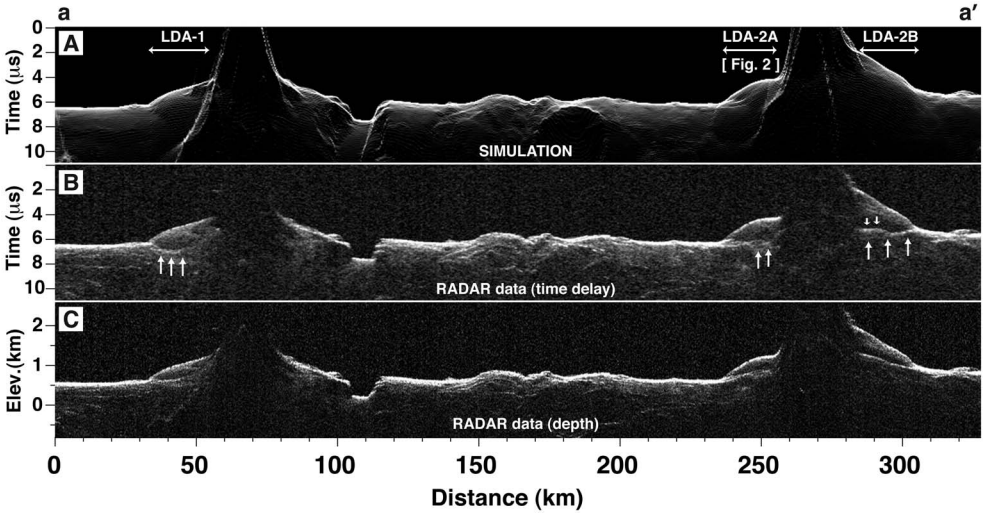

Fig. 3. Results for SHARAD orbit 6830 (line a-a′ in Fig. 1B). (**A**) Simulated surface echoes (clutter) in one-way travel time. (**B**) SHARAD data in one-way travel time. Vertical arrows identify echoes not consistent with surface clutter simulation and also confirmed in adjacent tracks. These echoes are interpreted to result from the subsurface. Radar returns are weak to nonexistent over steep massif slopes because of the scattering of energy away from the spacecraft. (**C**) Radar data converted to depth assuming a water-ice composition. All echoes appearing after the surface echo have new positions in this representation, including clutter.

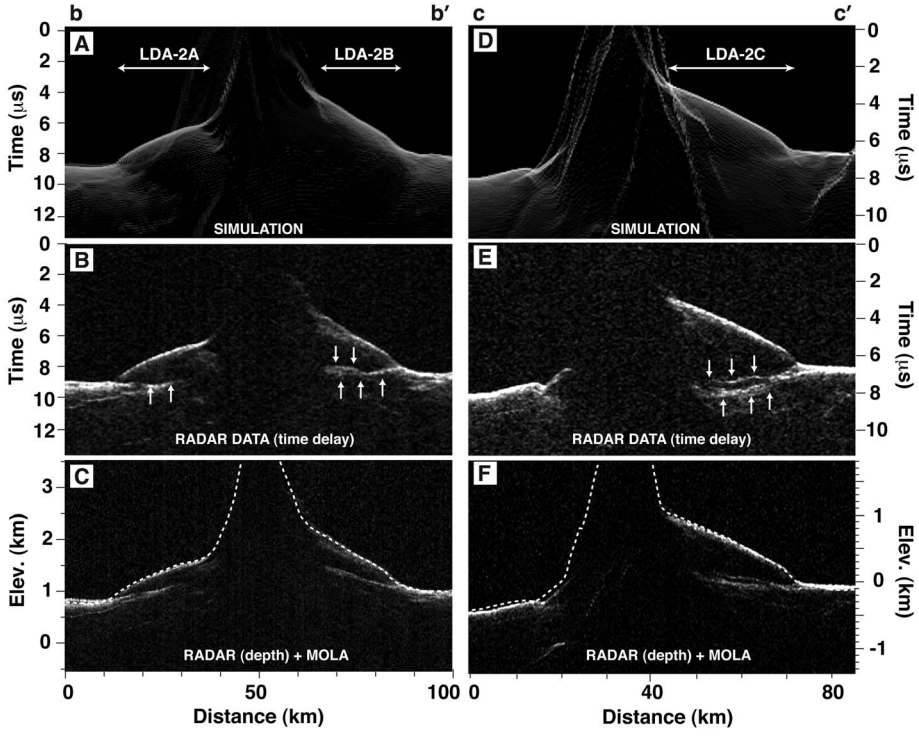

Fig. 4. Results for SHARAD orbits 7219 (left) and 3672 (right). Locations are indicated as b-b′ and c-c′ (Fig. 1B), respectively. (**A** and **D**) Simulated surface clutter. (**B** and **E**) SHARAD data with interpreted subsurface echoes denoted by vertical arrows. Both simulated and real data are shown in one-way travel time. (**C** and **F**) Radar data converted to depth using a wave velocity in water ice, with Mars Orbiter Laser Altimeter–derived surface elevations (*24*) superimposed (dashed white line). Note multiple reflectors near the base of LDA-2B and LDA-2C, confirmed by additional adjacent orbits, indicating thin basal deposits.

or the lower interface is too gradual to produce a detectable reflection. For the former case, we estimate the layer to be <10 m thick. The reflectors seen near the base of some deposits (Fig. 3B and Fig. 4, B and E) may be the result of thin layers of ice covered with debris similar to that seen at the upper surface.

With sufficient coverage, it will be possible to derive accurate regional estimates of total ice volume. On the basis of our findings and previous volume estimates from surface morphology (*6*), there may be up to ~28,000 km^3 of water ice sequestered in the eastern Hellas LDAs alone. This is ~1% of the total water volume contained in the polar caps (*24*) and is equivalent to a global water layer ~20 cm thick. For comparison, a much younger, meters-thick surface-mantling layer over much of the 30° to 60° latitude bands may contain an approximately equivalent volume of water in the form of interstitial ground ice (*25*). Subtle morphological differences observed among LDAs may be due to variations in ice content (*9*), and although the extension of radar studies to more LDAs is required to fully evaluate their potential range of compositions, preliminary results from Deuteronilus Mensae in the northern hemisphere corroborate our findings for eastern Hellas (*26*). Collectively, LDAs may therefore represent the largest reservoir of nonpolar water ice recognized on Mars.

Why would such large quantities of snow and ice accumulate in the eastern Hellas region in particular? Over time scales of millions of years, Mars undergoes large changes in spin-axis obliquity (*27*), forcing changes in insolation, and hence in climate (*28*) and the subsequent distribution of ice (*29*). Climate simulations (*30*) performed with a model that includes the current water cycle but assumes an obliquity of 45° predict snow accumulation in the eastern Hellas region from a south polar water source that operates efficiently at the southern summer solstice, when the southern polar cap releases large amounts of water vapor. This vapor moves northward and is deflected by cold air moving southward from the Hellas basin; the subsequent cooling causes strong condensation and precipitation in the area of the LDAs (*30*), which we have shown to contain primarily water ice. We therefore conclude that these deposits harbor large quantities of water ice derived from high-obliquity epochs, now concealed beneath a thin protective layer. This ice survives from climatic conditions markedly different from today's and is potentially accessible to future landed missions, not only for scientific study but as a resource to support exploration.

References and Notes

1. M. H. Carr, G. G. Schaber, *J. Geophys. Res.* **82**, 4039 (1977).
2. S. W. Squyres, *J. Geophys. Res.* **84**, 8087 (1979).
3. F. P. Fanale, J. R. Salvail, A. P. Zent, S. E. Postawko, *Icarus* **67**, 1 (1986).
4. M. H. Carr, *Water on Mars* (Oxford Univ. Press, New York, 1996).
5. B. K. Lucchitta, *J. Geophys. Res.* **89**, B409 (1984).
6. T. L. Pierce, D. A. Crown, *Icarus* **163**, 46 (2003).
7. J. W. Head *et al.*, *Nature* **434**, 346 (2005).
8. A. Colaprete, B. M. Jakosky, *J. Geophys. Res.* **103**, 5897 (1998).
9. H. Li, M. S. Robinson, D. M. Jurdy, *Icarus* **176**, 382 (2005).
10. N. Mangold, P. Allemand, *Geophys. Res. Lett.* **28**, 407 (2001).
11. J. W. Head *et al.*, *Earth Planet. Sci. Lett.* **241**, 663 (2006).
12. D. R. Marchant, J. W. Head III, *Icarus* **192**, 187 (2007).
13. J. W. Head, A. L. Nahm, D. R. Marchant, G. Neukum, *Geophys. Res. Lett.* **33**, L08S03 (2006).
14. A. M. Kress, J. W. Head III, D. R. Marchant, *Lunar Planet. Sci. Conf.* **39**, 1293 (2008).
15. R. Seu *et al.*, *J. Geophys. Res.* **112**, E05S05 (2007).
16. S. C. Mest, D. A. Crown, *Icarus* **153**, 89 (2001).
17. R. Seu *et al.*, *Science* **317**, 1715 (2007).
18. R. J. Phillips *et al.*, *Science* **320**, 1182 (2008); published online 13 May 2008 (10.1126/science.1157546).
19. J. W. Holt *et al.*, *J. Geophys. Res.* **111**, E06S24 (2006).
20. P. Gudmandsen, in *Electromagnetic Probing in Geophysics*, J. R. Wait, Ed. (Golem, Boulder, CO, 1971), pp. 329–333.
21. E. Heggy *et al.*, *Lunar Planet. Sci. Conf.* **38**, 1756 (2007).
22. G. Picardi *et al.*, *Science* **310**, 1925 (2005); published online 29 November 2005 (10.1126/science.1122165).
23. J. J. Plaut *et al.*, *Science* **316**, 92 (2007); published online 14 March 2007 (10.1126/science.1139672).
24. D. E. Smith *et al.*, *J. Geophys. Res.* **106**, 23689 (2001).
25. J. F. Mustard, C. D. Cooper, M. K. Rifkin, *Nature* **412**, 411 (2001).
26. J. J. Plaut *et al.*, *Lunar Planet. Sci. Conf.* **39**, 2290 (2008).
27. J. Laskar, P. Robutel, *Nature* **361**, 608 (1993).
28. J. Laskar *et al.*, *Icarus* **170**, 343 (2004).
29. J. W. Head *et al.*, *Nature* **426**, 797 (2003).
30. F. Forget, R. M. Haberle, F. Montmessin, B. Levrard, J. W. Head, *Science* **311**, 368 (2006).

31. We thank F. Russo, M. Cutigni, O. Fuga, and E. Giacomoni of the SHARAD Operations Center for their role in acquiring the data over these targets; F. Bernardini for his assistance in the U.S. data processing effort; and two anonymous reviewers for their comments and suggestions. Work at the University of Texas was supported by the Institute for Geophysics of the Jackson School of Geosciences and NASA grant NAG5-12693 (J.W.H.). MRO is operated for NASA by Caltech's Jet Propulsion Laboratory. SHARAD was provided to MRO by the Italian Space Agency through a contract with Thales Alenia Space Italia and is operated by the INFOCOM Department, University of Rome. This is UTIG contribution 2006.

Supporting Online Material

www.sciencemag.org/cgi/content/full/322/5905/1235/DC1
SOM Text
Fig. S1
References

5 August 2008; accepted 3 October 2008
10.1126/science.1164246

Variation in Evolutionary Patterns Across the Geographic Range of a Fossil Bivalve

Melissa Grey,[1]* James W. Haggart,[2,1] Paul L. Smith[1]

The fossil record is the only direct source of data for studying modes (patterns) and rates of morphological change over long periods of time. Determining modes and rates is important for understanding macroevolutionary processes, but just how modes and rates vary within a taxon, and why, remain largely unaddressed. We examined patterns of morphological change in the shell of the Mesozoic marine bivalve genus *Buchia* over its geographic and temporal range. Most modes conformed to either random walks or stasis, and both modes and rates showed variability between locations. For example, stasis was more common in deeper marine environments, whereas random walks occurred more often at the highest paleolatitudes studied. These results indicate that the environment can play an important role in shaping patterns of evolution.

Documenting patterns of morphological change (modes) and the speed at which they occur (rates) are fundamental to our understanding of macroevolutionary processes over geologic time. The fossil record has provided examples of three principal modes of evolution, namely: random walks; directional change (gradualism); and stasis, which is often interrupted by punctuated change. The ability to quantify rates and classify modes of evolution in the fossil record has improved over recent decades with the advent of quantitative model-based tests [e.g., (*1*–*4*)]. However, it remains virtually unknown whether modes and rates of evolution vary within a taxon, but this is difficult to assess because it requires large samples spanning both the geographic and temporal range of the taxon. *Buchia*, a marine bivalve distantly related to mussels, meets these requirements. The genus existed for ~25 million years, arising during the early Late Jurassic (155.6 million years ago) and becoming extinct in the Early Cretaceous (130.0 million years ago) (*5*), and includes numerous species that lived in a variety of sedimentary environments across the Northern Hemisphere (figs. S1 and S2). Most *Buchia* species are cosmopolitan

[1]Department of Earth and Ocean Sciences, University of British Columbia, Vancouver, British Columbia V6T 1Z4, Canada. [2]Geological Survey of Canada, 625 Robson Street, Vancouver, British Columbia V6B 5J3, Canada.

*To whom correspondence should be addressed. E-mail: mgrey@eos.ubc.ca